On the Morphology Changes of Al and Al-Cu Powder After Laser Melting



J.M. SKELTON, C.V. HEADLEY, E.J. SULLIVAN, J.M. FITZ-GERALD, and J.A. FLORO

Gas-atomized powders are commonly used in additive manufacturing, specifically laser powder bed fusion, due to their high flowability during recoating. Morphological changes can occur in particles that are irradiated by the laser during additive manufacturing, but are not incorporated into the melt pool. These irradiated particles will affect the rheology of the recycled powder in subsequent builds, potentially leading to failures due to uneven powder flow or spatial distribution. Thus, a better understanding of mechanisms that degrade the sphericity of powder after being laser irradiated is needed. This research examines morphological changes in Al and Al-Cu eutectic powders after laser melting. Two complementary approaches were taken. First, particles found along the edges of line scans following high-power (300 W) laser irradiation were characterized. The collected particles displayed morphological anomalies not observed in the as-received powder. Then, to gain a more quantitative and controlled perspective on morphological evolution, the same base powders were dispersed onto glass substrates and irradiated with a low-power (6.5 W) CW laser diode. This approach, which permits characterization of specific particles before and after laser irradiation, clearly shows laser-induced changes in the surface morphology of particles in the form of dents and rifts. These results suggest that isolated melting and resolidification of particles contained within their respective oxide shells can occur at the relatively low laser energy densities present at the edges of laser melt tracks. Thermal stresses developing in the oxide shell during cooling can account for the observed morphological changes in the context of shell-buckling theory.

https://doi.org/10.1007/s11663-020-01902-z © The Minerals, Metals & Materials Society and ASM International 2020

I. INTRODUCTION

IN the field of laser powder bed fusion (LPBF), much research has been focused on characterizing the changes that occur in the powder feedstock after laser irradiation in order to better understand the limitations of its powder recyclability. ^[1,2] The majority of these studies assume that all irradiated particles undergo melting and are incorporated into the melt pool of the laser track, focusing on the spatter that is ejected from the melt pool as the main source of defects in recycled powder. ^[3–6] However, very few consider particles on the peripheries of the laser track which have been irradiated, but not incorporated into the melt pool. If no sintering between neighboring particles occurs, this irradiated powder will end up being recycled and used in sequential builds. ^[7–10]

J.M. SKELTON, C.V. HEADLEY, E.J. SULLIVAN, J.M. FITZ-GERALD, and J.A. FLORO are with the Department of Materials Science and Engineering, University of Virginia, Charlottesville, VA 22903. Contact e-mail: jms3wp@virginia.edu Manuscript submitted January 14, 2020.

Article published online July 6, 2020.

Studies that focus on recycled powder are vital for the LPBF process since morphology irregularities of the particles could lead to failed builds due to uneven powder flow and spatial distribution. [11,12] Thus, a better understanding is needed on the mechanisms behind the morphological anomalies observed in recycled powder, especially those systems such as aluminum-based alloys that contain a tenacious native oxide shell that could pose a barrier to sintering. [3,13–15]

Recent studies have started to categorize the different types of particle morphologies found in recycled powder. For example, Popov *et al.*, identified thirteen different particle defects within the Ti-6Al-4V system, ranging from mechanically induced (broken particles) to agglomerates caused by spatter from the laser melt pool. [16] In order to better understand the formation of spatter-type defects within the AlSi10Mg system, Andani *et al.* used a highspeed camera to capture images of the laser melt pool in situ. [17] From this study, they proposed that both powder particles and liquid spatter were being jettisoned from the lasers path due to the recoil pressure of the laser. The nature of the jettisoned powder was not discussed further by Andani *et al.*, but a similar "partially heated" powder is brought

to attention by Asgari et al. on their study of the same system (AlSi10Mg). [14] In this study, only the large particles separated through sieving are thought to be affected by the laser and are assumed to be agglomerates, or "condensate", due to their large size and fine microstructure. It was suggested that the mechanism behind the formation of these large particles and their fine microstructure was related to the heating-cooling cycles and partial sintering between particles. In contrast to this conclusion, Lutter-Gunther et al. showed by isolating spatter from the feedstock powder that agglomerated particles originate from the laser melt pool. They then categorized spatter that solidified in air as spherical spatter and spatter that solidified on other particles as agglomerated spatter.^[3] It was also shown in this study that individual particles (non-agglomerated) were blown out of the melt pool, but little was done to characterize these particles to see how they had changed from the virgin powder.

Because it is common practice within the LPBF process to sieve powder with mesh sizes of below 70 μ m, most agglomerated particles will be removed from the recycled powder before reuse. [1,9,14] Thus, a degradation in the rheology of recycled powder is more likely to come from morphology changes of smaller, non-agglomerated particles.[18,19] Changes in the rheology between gas-atomized and plasma-atomized Ti alloy powders were attributed to slight differences in the sphericity of the particles by Yablokova et al., suggesting that even small alterations to the shape of spherical particles will lead to poor flowability.^[20] It becomes imperative then to understand how laser irradiation affects the morphology of powder that is neither incorporated into the melt pool nor formed into an agglomerate. Particles that fit into this category could potentially be found in the "blown powder" as well as along the sides of the melt pool, assuming a standard Gaussian power density distribution for the laser beam profile. In addition to this, powder alloys with naturally occurring oxides that could pose barriers to sintering and agglomeration may have a higher density of these non-agglomerated, heat-affected particles in the post-sieved powder. [13,15,21]

In this investigation, elemental Al and Al-Cu eutectic alloy powders are characterized before and after laser irradiation to assess and understand morphological changes that occur in the particles. It is suggested that particles on the edge of the laser melt pool can undergo melting and solidification during LPBF without incorporation into the melt pool or isolated agglomeration. The Al-Cu eutectic system is used in this study as a device to record the thermal history of the particles since changes in the two-phase microstructure can be observed through scanning electron microscopy (SEM). [22] To confirm that melting and solidification contributed to the morphological anomalies, individual particles are characterized both before and after laser irradiation. From these results, a direct correlation is made between laser irradiation and changes observed in particle surface morphology. It is shown that the retained oxide shell plays a crucial role in the prevention of sintering and the development of aspherical morphologies.

II. EXPERIMENTAL

Gas-atomized Al-33wt pctCu and elemental Al (99.8) wt pct) powders were obtained from Valimet Inc. with a mean particle diameter of $d_{50} = 20.33 \mu \text{m}$ and $d_{50} =$ 12.57 μ m, respectively. The Al-Cu eutectic powder was annealed in a box furnace (Thermolyne 48000) at 450 °C for 2 hours in order to obtain a uniformly coarse, two-phase microstructure. An SLM 125 equipped with a 400 W Yb-doped fiber optic laser ($\lambda = 1070$ nm, beam width = 100 μ m) from SLM Solutions Inc. and a 6.5 W solid-state laser diode ($\lambda = 450$ nm, beam width = 200 μm) from Endurance Lasers were used to irradiate powder samples in these experiments. Powder irradiation within the LPBF system was performed under an inert Ar environment (< 100 ppm oxygen) on a 5083 aluminum alloy substrate at a scan velocity of 1150 mm/ s and a laser power of 300 W. Samples were collected by stamping carbon tape over line scans on the build plate.

The low-power laser was used to irradiate particle arrays that were supported on glass slides, in an air ambient. Relatively dilute powder samples were prepared by drop casting onto glass slides using a solution of particles in DI water at a concentration of approximately 0.5 wt pct. The glass slides were previously coated with indium tin oxide (ITO) to promote electrical conductivity for improved SEM imaging that was performed before and after irradiation on the same regions of the specimens. An FEI LV650 SEM and Helios G4 DualBeam FIB were used to characterize the powder microstructure and morphology, including FIB milling to serially section particles to examine their internal microstructure.

III. RESULTS AND DISCUSSION

A. Base Powder Characterization

The as-received Al-Cu eutectic powder exhibited a range of eutectic microstructures as shown in Figure 1(a). These microstructural differences arose during gas atomization due to stochastic nucleation of the solid phase in the molten particles at varying undercoolings. An isothermal annealing of the powder was used to produce a coarsened two-phase microstructure uniformly across all particle sizes, with an average interphase spacing of 2 μ m shown in Figure 1(b).

Closer inspection of the annealed powder surface reveals faint lines superimposed on the annealed microstructure, which are believed to be the imprint of the as-received microstructure embossed on an oxide shell as seen in Figure 2.

These features could only be detected at probe currents below 7 kV within the SEM, suggesting that the secondary and backscattered electrons forming this signal were coming from a very thin surface layer. Both powder systems had satellite particles on the surface of larger particles, typical of gas-atomized powders. Elongated and irregularly shaped particles were infrequently observed within both powders. The elemental Al powder (Figure 3) exhibited a rougher surface morphology than the annealed Al-Cu powder (Figure 2). Both powders

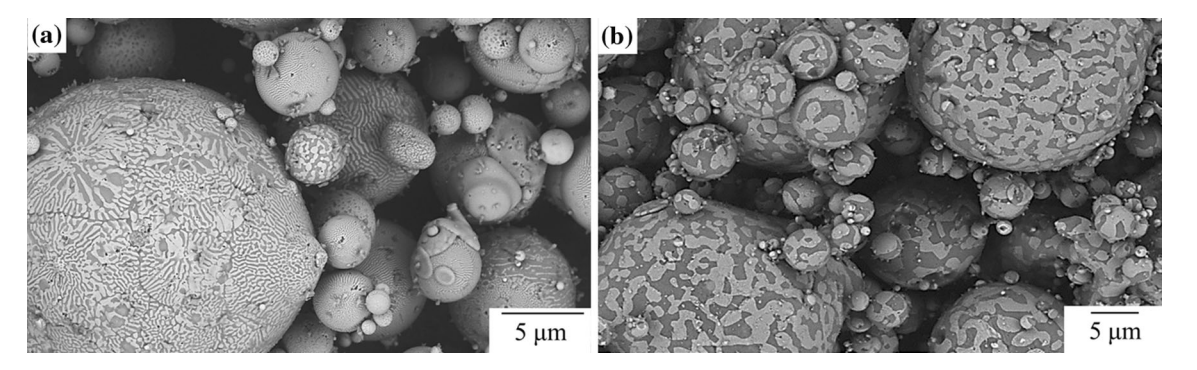


Fig. 1—As-received gas-atomized Al-33 wt pct Cu powder displaying fine eutectic microstructures (a). Powder annealed at 450 °C for 2 h showing uniformly coarsened eutectic microstructure (b).

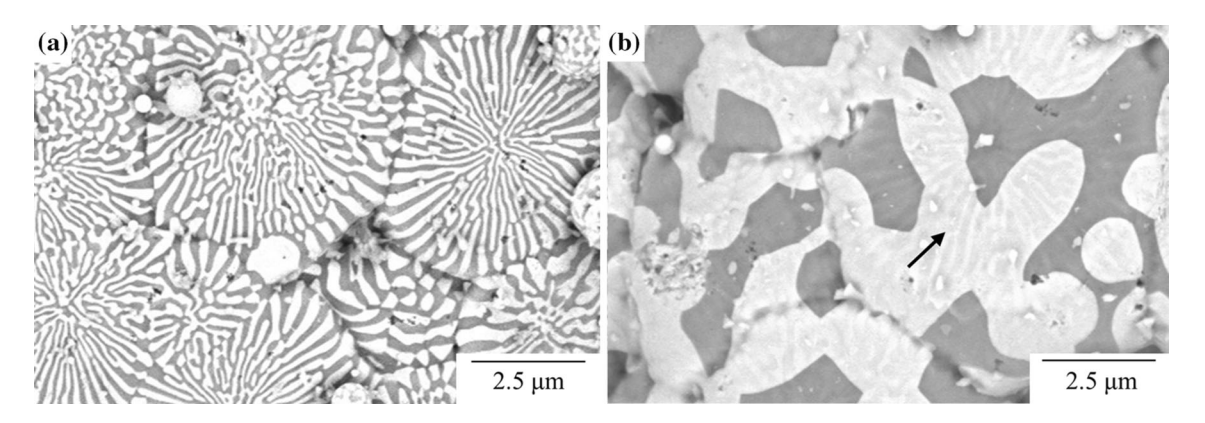


Fig. 2—Lamellar microstructure of as-received powder (a), coarse microstructure of annealed powder showing faint lines (black arrow) of original lamellar microstructure embossed on the oxide shell (b).

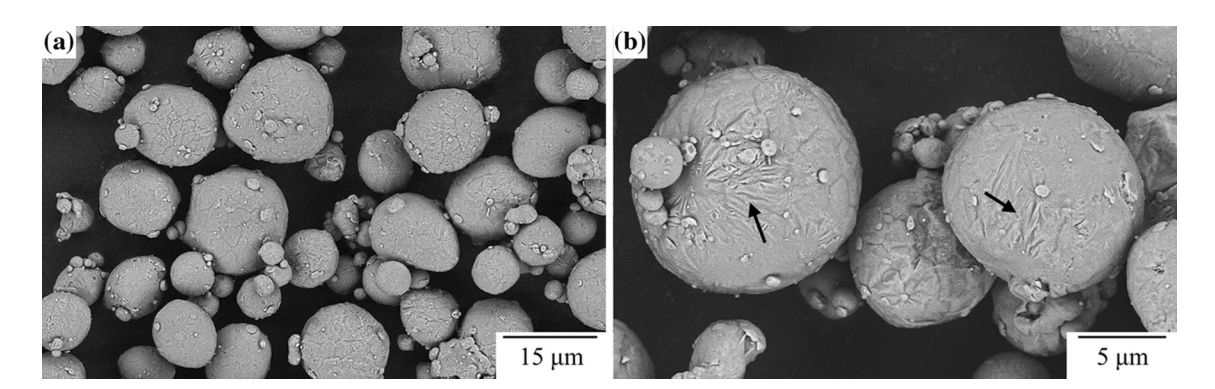


Fig. 3—As-received pure Al gas-atomized powder (a). Surfaces of many particles appear rough due to a wrinkling (black arrows) effect most likely occurring during the gas atomization process (b).

consisted of a low percentage of particles that contained dents on their surfaces, but none were observed with distinguishable cusps, or collapsed-like morphologies, such as what will be shown to form after laser melting.

B. Morphology Changes During LPBF

Processing parameters for line scans were chosen to be comparable with those found in literature for the manufacturing of Al10SiMg in the LPBF process, being one of the most commonly manufactured and studied

aluminum alloys in the field. [23–25] Powder collected from the vicinity of the line scan boundary in the Al powder showed large agglomerates (50 to 200 μ m) formed along the laser's scan path.

Since these larger particles would most likely be removed from the recycled powder during sieving, they were ignored, and smaller particles near the edge of the line scan were investigated. Morphological features not characteristic of the base powder were observed in small particles with diameters $< 20~\mu m$ near the edge of the laser path, with very little signs of agglomeration or

sintering between neighboring particles, as seen in Figure 4(a). Morphological abnormalities on smaller particles consisted of concave features circular in nature, defined here as *dents*, and narrow, collapsed-like features that contain an abrupt straight edge, defined here as *rifts*. Figure 4 shows examples of these dent and rift features, highlighting them with red and blue arrows, respectively.

Line scans were then performed in the Al-Cu powder at the same parameters and characterized in a similar manner. Large agglomerates were again observed, but approximately 5 times less frequently than in the pure Al. Due to the two-phase microstructure of this eutectic powder, a clear distinction could be made between particles that were close to the edge of the laser path with those that were farther away as seen in Figure 5.

The microstructure of the particles on the edge of the scan changed from the coarsened eutectic to a fine lamellar or dendritic structure. Morphologies distinct from the base powder could also be associated with these particles, with Figures 5(b) and (c) showing dent and rift features similar to those observed in the Al powder. To obtain a finer microstructure after laser irradiation, eutectic or dendritic solidification must occur, depending on the local solidification rate in each particle. As is well known in solidification theory, the lamellar eutectic period or the dendrite arm spacings are inversely related to both the undercooling and the solidification speed associated with the liquid/solid interface. [26] In powders, nucleation events depend strongly on the number of potential heterogeneous nucleation sites, such that the undercooling obtained in individual particles will be

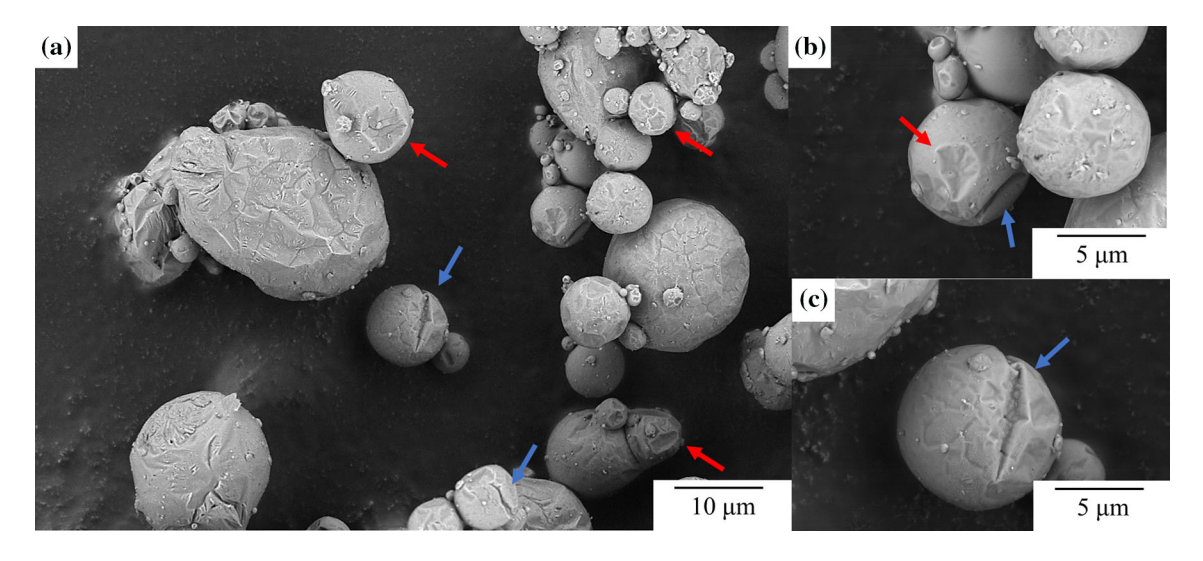


Fig. 4—Al powder collected on carbon tape around line scan performed at 300 W and 1150 mm/s, with large agglomerates clearly seen along laser path (a). Many particles at edge of line scan that did not agglomerate show morphological anomalies not typical of base powder, showing (b) dented (red arrows) and (c) rift-like (blue arrows) morphology.

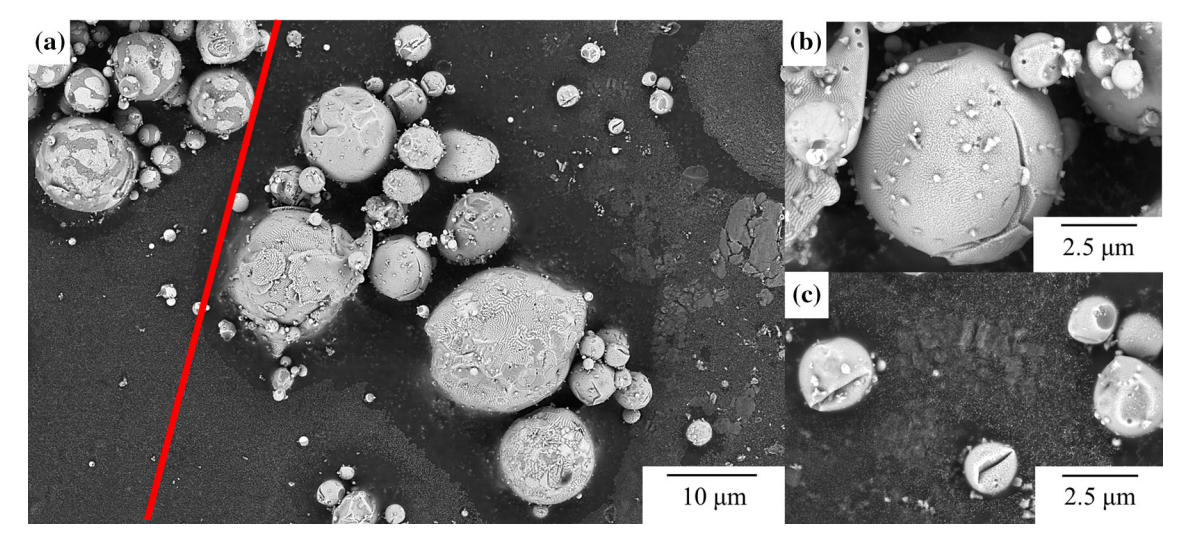


Fig. 5—Al-Cu eutectic powder collected on carbon tape around line scan at 300 W, 1150 mm/s. Powders collected at edge of line scan show a clear change in microstructure (right side of red line) from the coarsened base powder (left side of red line) (a). Closer inspection of irradiated particles shows signs of dented and rift-like morphology similar to those observed in the irradiated Al powder (b and c).

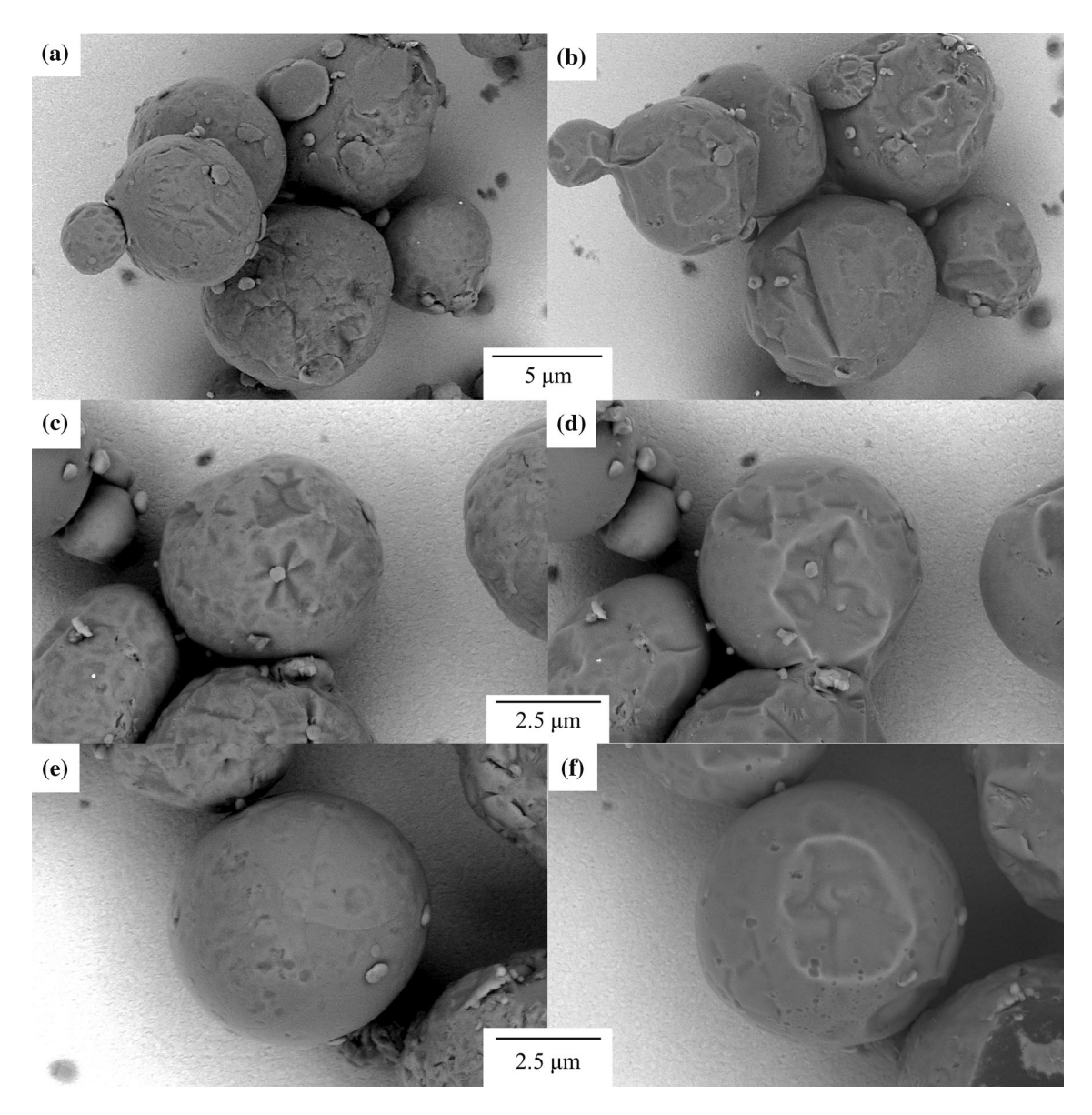


Fig. 6—Al powder on ITO-coated glass before laser irradiation (a, c, e) and after (b, d, f). Irradiated particles show dented or collapsed-like morphologies, with some displaying sharp rift-like features (b). Very little wetting is seen to occur between particles (b, d) most likely due to an oxide barrier. The spot size of the laser used was ca. 200 μ m, allowing for irradiation of all particles within each cluster.

stochastic. In addition to nucleation, differences in the local environment of the molten particle, such as the overall contact area with heat sinks, will also change the rate that heat is extracted and thus the solidification rate. It is therefore understandable (and observable) that the microstructure of the irradiated particles will vary, but that all particles that have undergone melting and solidification after laser irradiation will be distinct from the coarsened starting powder.

C. Characterization Before and After Low-Power Irradiation

To further investigate the morphology changes seen in the Al and Al-Cu particles along the edges of the line scans made using LPBF parameters, a model system was explored. Dilute powder dispersions on inert substrates

were prepared and the same sets of particles were characterized both before and after laser irradiation. Optically transparent and electrically conductive ITOcoated glass was used so that samples retained optical transparency while minimizing charging effects in the SEM without need for any additional coatings over the particles. A 6.5 W laser was used in these experiments at scan rates of 5 to 10 mm/s; the low power minimizes shock-induced movement of particles on the substrate. This lower power irradiation can be related to the local power density found at the edge of a high-powered laser with a Gaussian distribution beam profile, consistent with the LPBF system. The wavelength of this laser differs from that of the lasers used in the LPBF experiments. This could cause some quantitative changes in thermal transduction, but these are likely to be minor. These experiments permit before and after characterization of microstructure changes on the same particles, which provides deeper insight into the general mechanistic behaviors associated with the resolidification process, as will be shown and discussed below.

Characterization of the elemental Al powder in these experiments showed that morphology changes occurred as a result of laser irradiation, with dented and collapsed features appearing post irradiation as seen in Figure 6. No large agglomerates were observed in these experiments, with only limited sintering occurring between neighboring particles post irradiation as seen in Figures 6(b) and (d). Particle satellites often serve as useful fiducials to verify that identical regions on specific particles are being compared before and after laser melting.

By performing these same experiments with the Al-Cu powder, the mechanism behind these morphology changes could be better understood by observing the change in microstructure of the individual particles. As with the line scans performed in the LPBF system, the microstructure of the irradiated particles changed from the coarse eutectic structure to a fine lamellar or dendritic structure as shown in Figure 7. Minimal sintering was observed between particles, and the post-irradiated morphologies resembled those found in the experiments conducted with the Al powder. In addition, FIB cross-sections were taken of several irradiated Al-Cu particles to ensure that the fine eutectic structure was consistent throughout their bulk (refer to electronic supplementary material). By performing serial cross-sectioning on several particles, the solidification direction was able to be determined, which facilitated understanding of how these collapsed features arose, as discussed in the following sections.

To better understand trends in the observed morphologies, over 800 Al-Cu particles were counted and categorized according to their size and surface features (*i.e.*, spherical, dent, rift or sintered) as seen in Figure 8. The changes in the eutectic structure provide definitive proof that these particles underwent complete melting. It is clearly seen from this data that the majority of the irradiated particles in all size ranges displayed dent-like morphologies.

The normalized data in Figure 8(b) reveal that larger particles have a higher tendency to deform as the majority of particles in size ranges greater than 10 μ m were categorized as either dented or sintered. In addition, particles less than 10 μ m in diameter have a higher frequency of both rift and spherical morphologies. Particles that were irradiated and did not display a dent or rift feature were categorized as spherical, although many of these particles may have features hidden from view in the SEM. This same reasoning applies to particles that were categorized as sintered, with the possibility of hidden sintered particles existing in the sample that were not counted. Thus, for the spherical and sintered particles, the values displayed in Figure 8 represent the respective upper and lower bounds of these categories.

D. Origins of Morphological Change

Based on the experimental data, it is suggested that a native aluminum oxide on the surface of these particles forms a microcapsule that can serve as a containment vessel surrounding molten metal. Retention of a contiguous oxide shell supports many observations herein, including retention of discrete satellites even after melting of the primary particle, infrequent sintering, and surface "embossing" of the microstructure prior to melting (see Figure 2). Native oxide shells on Al alloys are inevitable, and the thickness of the native oxide of pure Al at room temperature in atmosphere stabilizes at ≤ 5 nm. [27] The eutectic Al-Cu powder is expected to have a thicker oxide on the order of 15 to 20 nm since it was heated in air at 450 °C for 2 hours. From the literature, it has been shown that furnace heating of pure Al under these conditions produces an oxide shell estimated to have a net thickness of 18 nm. [28] Interestingly, Al₂Cu is found to oxidize more readily than Al alone at room temperature, which could result in a locally thicker oxide above the θ phase. [29] An increased oxide thickness of the θ phase would explain the "embossed" pattern observed on the surface of the eutectic powder as seen in Figure 2(b).

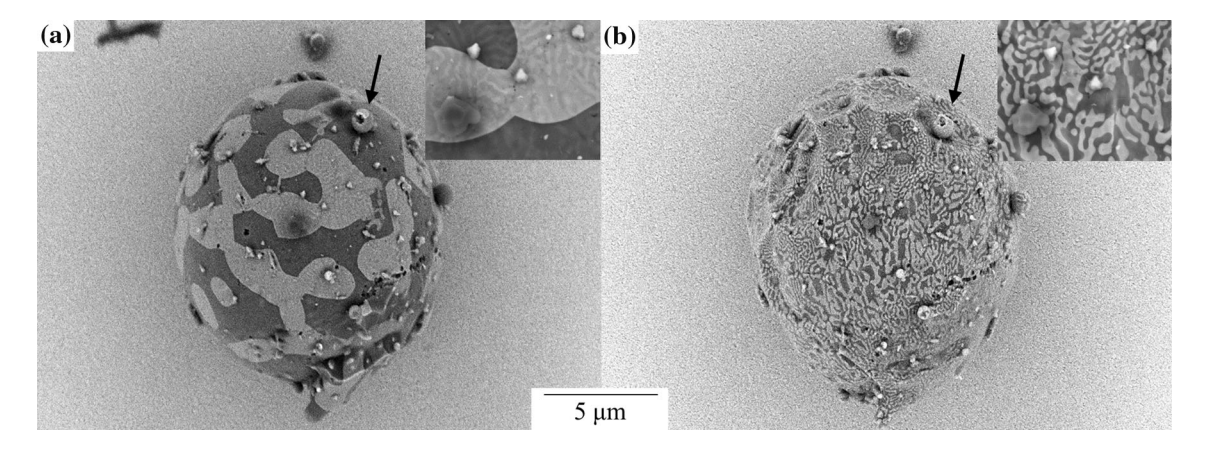


Fig. 7—Isolated 10 μ m particle before laser irradiation (a) and after (b). Satellite particles are found in the same position on surface of particle after laser irradiation (black arrow) with no agglomeration taking place.

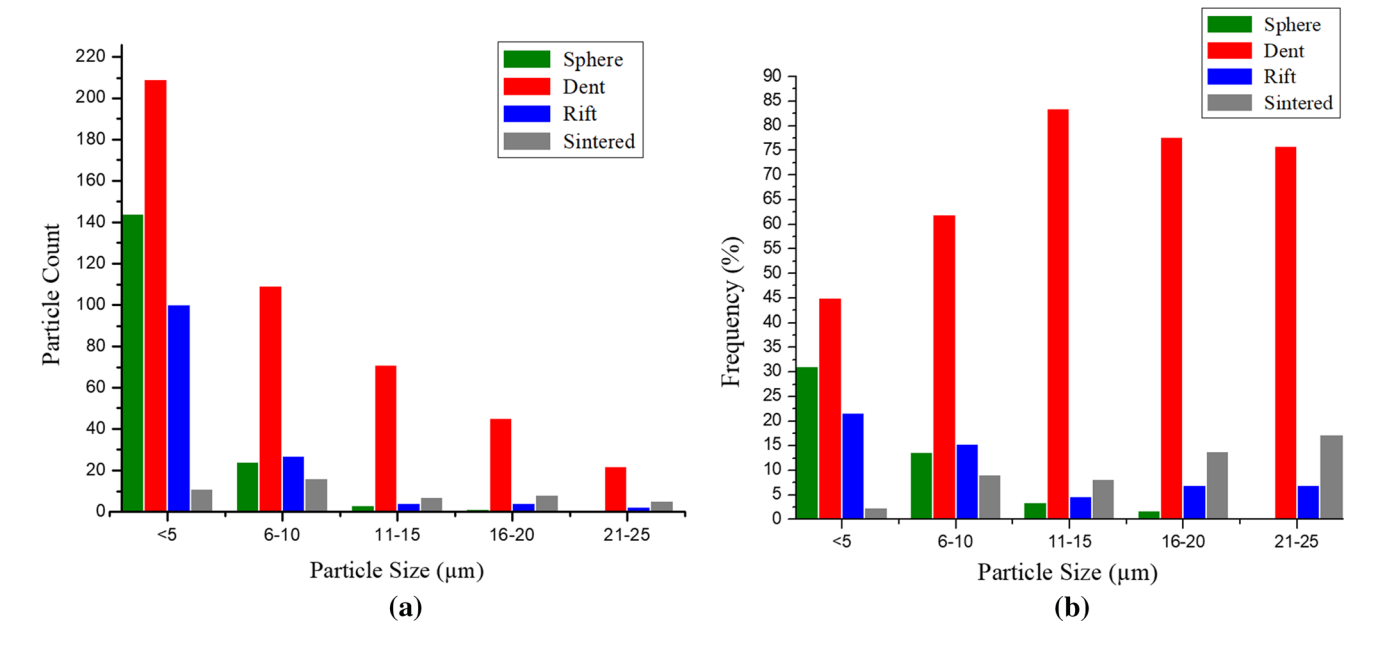


Fig. 8—Number of irradiated Al-Cu particles observed to display either a spherical, dented, or rift-like morphology, as well as those that were sintered together, categorized by size (a). Normalized data showing trends in the occurrence of different morphologies, such as a higher percentage of particles with spherical and rift morphologies occurring in smaller particles, while larger particles appear to have a higher occurrence of sintering events (b).

The major morphological changes in resolidified Al and Al-Cu powders, e.g., dents and rifts, can be attributed to the presence of an oxide shell. Upon heating of a particle during laser irradiation, the metal undergoes thermal expansion in both the solid and liquid phases, as well as expansion at the melting point due to density differences in the two phases. For example, the total expansion expected in pure Al going from room temperature to just above the melting temperature (~ 660 °C) is 11 pct calculated by the change in density. [30] Since the oxide shell will have a much lower thermal expansion for the same thermal excursion, 0.8 pct for amorphous alumina, the shell will be placed in tension. [31] This can lead to fracture and spalling of the oxide, which is observed under more intense melting conditions. However, at lower laser power densities, the shell is retained. It is hypothesized here that the oxide shell can accommodate the strain induced by the thermal expansion of the particle during the heating cycle by rapid oxide re-growth in an air or partial oxygen environment. Validation for dynamic oxide re-growth on these timescales was observed from recent work performed by Yang et al., whose in situ TEM experiments captured real-time growth of amorphous alumina over an exposed aluminum surface during deformation. [32] The growth rate was determined to be approximately 0.25 nm/s, at an O_2 pressure of 3.6 \times 10⁻⁶ Torr and room temperature. [32] Using standard expressions for molecular arrival rate in a gas vs. pressure, and the idealized structure of corundum to estimate monolayer densities and thicknesses, the maximum growth rate (the rate associated with complete reaction of all arriving oxygen to form Al₂O₃) is given by $G_{\text{max}}(\text{nm/s}) = 9.1 \times 10^{5} \text{*P (Torr)}$. For the pressures used by Yang et al., this predicts G about 10× larger than measured by them, reflecting sluggish reaction/diffusion kinetics at room temperature. For an O_2 partial pressure of 0.1 Torr (more typical of the LBPF environment), the maximum growth rate is 9×10^4 nm/s. Re-growth of a 10 nm oxide in 1 msec would require a rate of only 1×10^4 nm/s, so the oxygen supply is 9 times larger than what is needed, suggesting that oxide re-growth is not supply limited. Rates are much higher than Yang et al., both because of the much higher oxygen supply, and because of the much higher temperatures reached during laser melting. Hence it seems quite reasonable that the oxide can dynamically grow along tears or ruptures that occur in the shell, effectively self-healing and continuously conforming to the thermally expanding powder particles during laser heating.

If the oxide shell dynamically heals during the heating and melting cycle as discussed above, then at the maximum temperature, the shell can be assumed to be strain free. Upon cooling and resolidification, the rapid contraction of the metal particle then places the oxide shell under a state of inward-directed hydrostatic pressure. [33–35] This assumes that the liquid metal wets the oxide and does not pull away from the shell as it contracts. Buckling of the shell into the molten metal would lead to the dent or rift features seen frequently in this work. A standard expression for the pressure required to create buckling in a perfect spherical shell is:

$$P_{\rm c} = \left(\frac{2E}{\sqrt{3(1-v^2)}}\right) \left(\frac{h}{R}\right)^2$$
 [1]

where E is the Young's modulus, v is Poisson's ratio, h is the thickness of the oxide shell and R is the particle radius.^[36] Unsurprisingly, thinner shell walls, or larger

shell diameters (here, the particle diameter), will buckle more readily. Note that for an oxide shell with E=300 GPa, $\nu=0.21$, h=20 nm and R=5 μ m, then $P_{\rm c}=5.7$ MPa.

Dewetting of the molten Al to leave a vacuum gap under the oxide shell would not result in buckling, since the external pressure $P_{\rm ext}=1$ atm = 0.1 MPa $<< P_{\rm c}$. This supports the contention above that the contractile liquid metal wets the oxide shell and places it under hydrostatic compression during cooling. That said, voids or entrapped gas already present within the particle as a result of being gas atomized may cause pockets to form between the liquid core and the oxide shell (see Supplementary Figure S-2). This scenario does not appear to be the norm though and is not further considered here.

The standard expression for the radial strains in the thin shell limit, expressed in spherical coordinates, is:

$$\varepsilon_{\rm rr} = \left(\frac{\Delta P \nu}{E}\right) \left(\frac{R}{h}\right)$$
[2]

where ΔP is the pressure differential across the shell wall. Equating the strain to the thermal strain, $\Delta \alpha \Delta T$, where $\Delta \alpha$ is the difference in thermal expansion coefficient between the metal and oxide, and $\Delta P = P_{\rm c}$ from Eq. [1], allows the required temperature change for differential thermal expansion to buckle the shell to be obtained:

$$\Delta T = \frac{2v}{\Delta \alpha \sqrt{3(1-v^2)}} \left(\frac{h}{R}\right)$$
 [3]

Taking v = 0.22 for alumina, $\Delta \alpha = 2.1 \times 10^{-5}$ (alumina vs. aluminum) and the oxide shell thickness to be 10 nm, yields $\Delta T_{\rm c} = 124/{\rm R}$, where the particle radius, R, is expressed in $\mu {\rm m.}^{[31,38]}$ For example, a powder particle with a 2 $\mu {\rm m}$ radius requires a cooling of 62 °C from the maximum temperature to produce the critical strain for buckling. This seems eminently reasonable for laser melting, but note that Eq. [1] is well known to over-predict the critical pressure for buckling by 2 to 6× due to imperfections in real shells. [39] Hence the required temperature excursion may be only of order 10 °C to 30 °C for buckling to form dents, and even less in larger particles. The data of Figure 8 show that the likelihood of dent formation increases as the particle size, and therefore R/h, increases (at least until sintering starts to become significant), consistent with predictions of buckling theory.

Dent and rift morphologies are "post-buckling" instabilities associated with pressures exceeding the critical value, which are frequently observed in pressure vessels of all shapes and sizes. [40] Dents are envisioned here to form during cooling of the superheated liquid prior to solidification. They can continuously enlarge with thermal contraction as the liquid cools towards the melting temperature (or even supercools below the melting point). They can also enlarge by coalescence of two or more smaller dents. [41]

The solidification process likely influences the formation of dent and rift structures. Solidification of a liquid within a spherical shell has been shown to produce morphologies analogous to those observed here, as shown by Yu et al., in their study of microencapsulated phase-change material slurries. [42] Solidification induces large additional strains due to the density increase and breaks the spherical symmetry ahead of a propagating solid/liquid interface. For example, the advancing solidification front might force coalescence of smaller dents or buckling modes into larger dents opposite the front. Evidence for this "plowing" mechanism was obtained by serial cross-sectioning (See Supplementary Figures S-1 and S-2). The microstructure indicates where solid phase nucleated and the approximate shape of the advancing interface. The external surfaces of many particles near the solid nucleation site is smooth, while the surface furthest away from the nucleation site (last region to solidify) exhibits a higher concentration of dents. This strongly suggests that solidification plays a key role in the final morphology of these particles.

Interestingly, Figure 8 shows that rifts tend to occur more often in smaller particles, which is not expected a priori from Eq. [1]. Two possible scenarios may explain why smaller particles are more likely to rift during solidification. First, smaller particles are more likely to contain only a single nucleation event, evident by the many single grain particles found with diameter ranges of $< 5 \mu m$ in this study. The advancing solid/liquid interface breaks symmetry as discussed above, creating more localized stresses in the shell. Smaller particles have a larger h/R value that can allow larger stresses to develop, and in cases when only one nuclei forms, these stresses may concentrate in the shell above the last of the liquid to solidify, leading to catastrophic failure in the form of a rift (see Supplementary Figure S-3). A schematic of how dents and rifts may occur in different particle sizes can be seen in Figure 9. Larger particles, with multiple nucleation sites may solidify on the surface too rapidly for deep rifts to form. The second possible contributor towards skewing prevalence of rifts in smaller particles is a difference in solidification rate that occurs between smaller and larger particles. Because smaller particles will have on average fewer potential nucleation sites, they are more likely to experience greater undercoolings and larger solidification rates relative to larger particles. Evidence for this can be observed in Figure 1(a) where smaller particles ($< 5 \mu m$) typically have finer length scales in their solidification microstructure than larger particles. Faster solidification rates imply higher strain rates in the oxide shells, which can enhance tendencies for more extreme buckling. [43]

While there are other possible explanations for the morphological changes observed here, the large-scale effect of distributed voids in the powder particles is rejected since the pressure on a void would not initiate collapse. Sectioning of as-received particles gave further evidence that the void volume is insufficient to account for the amount of collapse observed here. Dents in

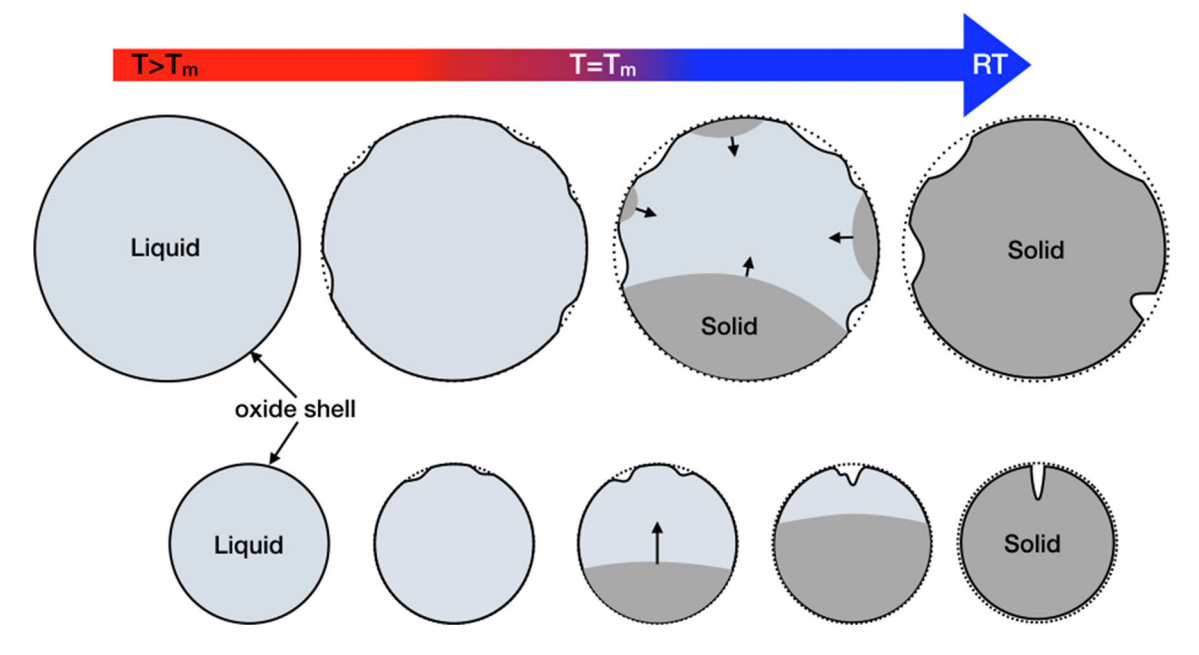


Fig. 9—Schematic illustration of the proposed mechanism for formation of the dent and rift morphologies observed in irradiated particles. Buckling can occur in the shell while the particle is still molten due to differential thermal contraction. These buckles can sometimes coalesce during solidification, *e.g.*, being pushed together by the advancing solid/liquid interface. As described in the text, particle size may influence the number of solid nucleation sites and the velocity of the solidification front.

particles could result from local Hertzian contact between adjacent particles during melting. However, SEM micrographs taken before and after laser processing clearly showed that the dents cannot be attributed to local mechanical contact. Laser induced shockwaves and Marangoni effects often can create extreme morphologies. However, the oxide entrainment of the liquid is not consistent with this. For example, it is frequently observed that satellite particles survive local surface collapse without ejection or other obvious movement.

IV. CONCLUSION

The morphological changes occurring in Al and Al-Cu powders after laser irradiation have been studied and a mechanism explaining the cause of these changes is proposed. It has been shown through the use of the eutectic microstructure in Al-Cu that the majority of particles that undergo low-power irradiation melt and resolidify without agglomeration or sintering, and that this can occur under standard processing parameters during LPBF along the edges of each track. Characterization of particles before and after low-power laser irradiation clearly demonstrate that the dent and rift features observed in irradiated particles are morphologies resulting from solidification coupled with buckling of the oxide shell. It is proposed that the oxide layer around each particle acts as a microcapsule that can prevent sintering, while thermal stresses lead to buckling of the shell.

Pertinent to additive manufacturing, these results explain how morphological anomalies may arise in recycled powder feedstocks with robust oxides in lieu of the more commonly studied agglomeration and spatter defects. Furthermore, it has been shown that a dynamically healing oxide can suppress contiguous melting and even local sintering between particles, specifically along the track periphery where the laser power density is low. Powder particles that are not fully subsumed into the build will deform, and if these particles are recycled, they will impact the subsequent powder rheology, potentially leading to additional build defects. Thus, while larger spatter or agglomerate defects will be removed during sieving, particles with collapsed morphologies will retain sizes equivalent to the virgin powder, causing them to be inextricable from the recycled powder. Therefore, it is believed that these morphology changes may play a critical role in the degradation of recycled powder that has hitherto been overlooked.

ACKNOWLEDGMENTS

Support from the National Science Foundation under award NSF-1663085 is gratefully acknowledged. Utilization of the FEI LV650 SEM and FEI Helios G4 DualBeam within UVa's Nanoscale Materials Characterization Facility (NMCF) was crucial to this work. Special thanks to Cathy Dukes for her helpful discussions.

ELECTRONIC SUPPLEMENTARY MATERIAL

The online version of this article (https://doi.org/10.10 07/s11663-020-01902-z) contains supplementary material, which is available to authorized users.

REFERENCES

- A. Strondl, O. Lyckfeldt, H. Brodin, and U. Ackelid: Miner. Met. Mater. Soc., 2015, vol. 37, pp. 549–54.
- A.H. Maamoun, M. Elbestawi, G.K. Dosbaeva, and S.C. Veldhuis: Addit. Manuf., 2018, vol. 21, pp. 234–47.
- M. Lutter-Günther, M. Bröker, T. Mayer, S. Lizak, C. Seidel, and G. Reinhart: *Procedia CIRP*, 2018, vol. 74, pp. 33–38.
 V. Gunenthiram, P. Peyre, M. Schneider, M. Dal, F. Coste, I.
- V. Gunenthiram, P. Peyre, M. Schneider, M. Dal, F. Coste, I. Koutiri, and R. Fabbro: *J. Mater. Process. Technol.*, 2018, vol. 251, pp. 376–86.
- D. Wang, S. Wu, F. Fu, S. Mai, Y. Yang, Y. Liu, and C. Song: Mater. Des., 2017, vol. 117, pp. 121–30.
- C.L.A. Leung, S. Marussi, M. Towrie, R.C. Atwood, P.J. Withers, and P.D. Lee: *Acta Mater.*, 2019, vol. 166, pp. 294–305.
- 7. J.A. Slotwinski and E.J. Garboczi: *Jom*, 2015, vol. 67, pp. 538–43.
- 8. J.A. Slotwinski, E.J. Garboczi, P.E. Stutzman, C.F. Ferraris, S.S. Watson, and M.A. Peltz: *J. Res. Natl. Inst. Stand. Technol.*, 2014, vol. 119, pp. 460–93.
- L.C. Ardila, F. Garciandia, J.B. González-Díaz, P. Álvarez, A. Echeverria, M.M. Petite, R. Deffley, and J. Ochoa: *Phys. Procedia*, 2014, vol. 56, pp. 99–107.
- D. Wang, G. Ye, W. Dou, M. Zhang, Y. Yang, and S. Mai: Opt. Laser Technol., 2020, vol. 121, p. 105678.
- 11. J. Clayton, D. Millington-Smith, and B. Armstrong: Jon, 2015, vol. 67, pp. 544–48.
- J.H. Tan, W.L.E. Wong, and K.W. Dalgarno: Addit. Manuf., 2017, vol. 18, pp. 228–55.
- E. Louvis, P. Fox, and C.J. Sutcliffe: *J. Mater. Process. Technol.*, 2011, vol. 211, pp. 275–84.
- 14. H. Asgari, C. Baxter, K. Hosseinkhani, and M. Mohammadi: *Mater. Sci. Eng. A*, 2017, vol. 707, pp. 148–58.
- M. Simonelli, C. Tuck, N.T. Aboulkhair, I. Maskery, I. Ashcroft, R.D. Wildman, and R. Hague: *Metall. Mater. Trans. A*, 2015, vol. 46A, pp. 3842–51.
- V.V. Popov, A. Katz-Demyanetz, A. Garkun, and M. Bamberger: Addit. Manuf., 2018, vol. 22, pp. 834–43.
- M. Taheri Andani, R. Dehghani, M.R. Karamooz-Ravari, R. Mirzaeifar, and J. Ni: Addit. Manuf., 2018, vol. 20, pp. 33–43.
- F. Ahmed, U. Ali, D. Sarker, E. Marzbanrad, K. Choi, Y. Mahmoodkhani, and E. Toyserkani: J. Mater. Process. Technol., 2020, vol. 278, p. 116522.
- H. Gruber, P. Karimi, E. Hryha, and L. Nyborg: *Powder Metall. Prog.*, 2018, vol. 18, pp. 40–48.
- G. Yablokova, M. Speirs, J. Van Humbeeck, J.P. Kruth, J. Schrooten, R. Cloots, F. Boschini, G. Lumay, and J. Luyten: Powder Technol., 2015, vol. 283, pp. 199–209.

- M. Simonelli, N.T. Aboulkhair, P. Cohen, J.W. Murray, A.T. Clare, C. Tuck, and R.J.M. Hague: *Mater. Charact.*, 2018, vol. 143, pp. 118–26.
- B.A. Mueller and J.H. Perepezko: *Mater. Sci. Eng.*, 1988, vol. 98, pp. 153–56.
- J.H. Martin, D. Yahata, J.M. Hundley, J.A. Mayer, T.A. Schaedler, and T.M. Pollock: *Nature*, 2017, vol. 549, pp. 365–69.
- 24. S. Dadbakhsh and L. Hao: *J. Alloys Compd.*, 2012, vol. 541, pp. 328–34. https://doi.org/10.1016/j.jallcom.2012.06.097.
- F. Trevisan, F. Calignano, M. Lorusso, J. Pakkanen, A. Aversa, E.P. Ambrosio, M. Lombardi, P. Fino, and D. Manfredi: *Materials.*, 2017, vol. 10, pp. 1–23. https://doi.org/10.3390/ma10010076.
- W. Kurz and D.J. Fisher: Fundamentals of Solidification, Trans Tech Publications LTD, Fourth Rev., 1998.
- M.T.A. Saif, S. Zhang, A. Haque, and K.J. Hsia: *Acta Mater.*, 2002, vol. 50, pp. 2779–86.
- 28. W.W. Smeltzer: J. Electrochem. Soc., 1956, vol. 103, pp. 209–14.
- K.A. Son, N. Missert, J.C. Barbour, J.J. Hren, R.G. Copeland, and K.G. Minor: J. Electrochem. Soc., 2001, vol. 148, pp. 260–3.
- M. Leitner, T. Leitner, A. Schmon, K. Aziz, and G. Pottlacher: Metall. Mater. Trans. A, 2017, vol. 48A, pp. 3036–45.
- D.C. Miller, R.R. Foster, S.H. Jen, J.A. Bertrand, S.J. Cunningham, A.S. Morris, Y.C. Lee, S.M. George, and M.L. Dunn: Sens. Actuators A, 2010, vol. 164, pp. 58–67.
- Y. Yang, A. Kushima, W. Han, H. Xin, and J. Li: *Nano Lett.*, 2018, vol. 18, pp. 2492–97.
- 33. M. Ksiazek, N. Sobczak, B. Mikulowski, W. Radziwill, and I. Surowiak: *Mater. Sci. Eng. A*, 2002, vol. 324, pp. 162–67.
- 34. A.J. Klinter, G. Mendoza-Suarez, and R.A.L. Drew: *Mater. Sci. Eng. A*, 2008, vol. 495, pp. 147–52.
- 35. E.N. Coker: Sandia Rep. Sandia Natl. Lab., 2013, pp. 1–22.
- J.W. Hutchinson: Proc. R. Soc. A, 2016, vol. 472, p. 20160577. https://doi.org/10.1098/rspa.2016.0577.
- 37. S.P. Timoshenko and J.M. Gere: *Theory of Elastic Stability*, 2nd ed., McGraw Hill, New York, 1961.
- 38. P. Hidnert: Sci. Pap. Bur. Stand., 1924, vol. 19, p. 697.
- 39. C. Hutchinson, X. Fan, S. Pennycook, and G. Shiflet: *Acta Mater.*, 2001, vol. 49, pp. 2827–41.
- 40. J. Błachut: Appl. Mech. Rev., 2014, vol. 66, pp. 30-33
- G.A. Vliegenthart and G. Gompper: New J. Phys., 2011, vol. 13, p. 045020. https://doi.org/10.1088/1367-2630/13/4/045020.
- 42. Q. Yu, F. Tchuenbou-Magaia, B. Al-Duri, Z. Zhang, Y. Ding, and Y. Li: *Appl. Energy*, 2018, vol. 211, pp. 1190–202.
- 43. P. Li, N. Petrinic, and C.R. Siviour: *Mech. Mater.*, 2012, vol. 54, pp. 43–54.
- 44. C.S. Montross, T. Wei, L. Ye, G. Clark, and Y.W. Mai: *Int. J. Fatigue*, 2002, vol. 24, pp. 1021–36.
- 45. C. Qiu, C. Panwisawas, M. Ward, H.C. Basoalto, J.W. Brooks, and M.M. Attallah: *Acta Mater.*, 2015, vol. 96, pp. 72–79.
- 46. H.J. Niu and I.T.H. Chang: *J. Mater. Sci.*, 2000, vol. 35, pp. 31–38.

Publisher's Note Springer Nature remains neutral with regard to jurisdictional claims in published maps and institutional affiliations.